

Reversible multi-electron redox chemistry of π -conjugated N-containing heteroaromatic molecule-based organic cathodes

Chengxin Peng^{1†}, Guo-Hong Ning^{1†}, Jie Su^{1†}, Guiming Zhong², Wei Tang¹, Bingbing Tian¹, Chenliang Su¹, Dingyi Yu¹, Lianhai Zu³, Jinhu Yang³, Man-Fai Ng⁴, Yong-Sheng Hu⁵, Yong Yang^{2*}, Michel Armand⁵ and Kian Ping Loh^{1*}

Even though organic molecules with well-designed functional groups can be programmed to have high electron density per unit mass, their poor electrical conductivity and low cycle stability limit their applications in batteries. Here we report a facile synthesis of π -conjugated quinoxaline-based heteroaromatic molecules (3Q) by condensation of cyclic carbonyl molecules with *o*-phenylenediamine. 3Q features a number of electron-deficient pyrazine sites, where multiple redox reactions take place. When hybridized with graphene and coupled with an ether-based electrolyte, an organic cathode based on 3Q molecules displays a discharge capacity of 395 mAh g⁻¹ at 400 mA g⁻¹ (1C) in the voltage range of 1.2–3.9 V and a nearly 70% capacity retention after 10,000 cycles at 8 A g⁻¹. It also exhibits a capacity of 222 mAh g⁻¹ at 20C, which corresponds to 60% of the initial specific capacity. Our results offer evidence that heteroaromatic molecules with multiple redox sites are promising in developing high-energy-density, long-cycle-life organic rechargeable batteries.

With the increasing demand for large-scale battery systems in electric vehicles (EVs) and smart renewable energy grids, the prospect of using organic materials as electrodes in rechargeable batteries has become increasingly attractive. Organic electrode materials have lower environmental footprints, greater safety as compared to inorganic metal oxide electrodes, and allow eco-efficient production and disposal¹. In addition to being light, organic electrodes afford high energy storage capabilities since their structures can be engineered at the molecular level to support multiple redox reactions². Organic molecules with appropriately designed functional groups are electroactive towards lithium^{2–8} as well as some earth-abundant metals such as sodium^{9,10}, magnesium¹¹, aluminium¹² and zinc¹³. Not surprisingly, electroactive organic molecules are now being actively explored as energy storage systems in supercapacitors^{14,15}, thin-film batteries¹⁶, aqueous rechargeable batteries¹⁷, lithium air batteries¹⁸, and redox flow batteries^{19–22}.

Conductive polymers^{23–25}, organosulfur compounds^{26,27}, stable radical compounds^{3,22,28,29}, and organic carbonyl compounds based on oxalate salts and quinone/phenoxide derivatives^{2,4,6,8,10,30–33} have been used as electrodes in rechargeable lithium/sodium ion batteries. However, the dissolution of these organic active compounds in aprotic electrolytes causes rapid capacity fading during cycling. Various strategies have been proposed to suppress the dissolution of the organic electrode (Fig. 1a). These include attaching the electroactive molecule covalently to a conductive backbone³⁴, polymerizing the redox-active compound^{4,6}, and

forming a salt with organic carbonyl compounds^{2,33}. Another challenge facing organic-based electrodes is the unimpressive power capability due to the low intrinsic electrical conductivity of organic molecules^{2,35}. π -conjugated aromatic compounds containing heteroatoms (for example, O, N, and S) with a lone pair of electrons demonstrate good redox activity and can be utilized as electroactive materials for rechargeable batteries. Among these, nitrogen-containing heteroaromatic compounds such as polymeric Schiff bases³⁶, indigo carmine³⁷, or pteridine⁵, have been explored for this purpose. To develop high-energy and high-power-density rechargeable batteries, we need to design organic molecules with multiple redox centres and high intrinsic electrical conductivity.

At a fundamental level, it is important to understand the dynamics of the multiple redox reactions and associated structural evolutions during the redox reactions, and to determine the maximum number of electrons transferred during battery operations. This knowledge provides the foundation for the design of advanced electrode materials with improved energy densities³⁸. However, mechanistic studies are hampered by the amorphous nature of most organic materials, which precludes the use of structural characterization techniques such as X-ray diffraction (XRD) and transmission electron microscopy (TEM)³⁹.

Inspired by the extended π -conjugated system of high-mobility organic semiconductors, here we develop fused N-heteroaromatic triquinoxalinyne molecules (3Q) which can be used as cathode in rechargeable organic batteries (Fig. 1b). The multiple electroactive

¹Department of Chemistry, Centre for Advanced 2D Materials and Graphene Research Centre, National University of Singapore, 3 Science Drive 3, Singapore 117543, Singapore. ²State Key Laboratory of Physical Chemistry of Solid Surfaces, Department of Chemistry, College of Chemistry and Chemical Engineering, Collaborative Innovation Center of Chemistry for Energy Materials (iChEM), Xiamen University, Xiamen 361005, China. ³Department of Chemistry, Tongji University, Siping Road 1239, Shanghai 200092, China. ⁴Institute of High Performance Computing, Agency for Science, Technology and Research, 1 Fusionopolis Way, #16-16 Connexis, Singapore 138632, Singapore. ⁵Key Laboratory for Renewable Energy, Beijing Key Laboratory for New Energy Materials and Devices, Beijing National Laboratory for Condensed Matter Physics, Institute of Physics, Chinese Academy of Sciences, School of Physical Sciences, University of Chinese Academy of Sciences, Beijing 100190, China. [†]These authors contributed equally to this work.

*e-mail: yyang@xmu.edu.cn; chmlpkp@nus.edu.sg

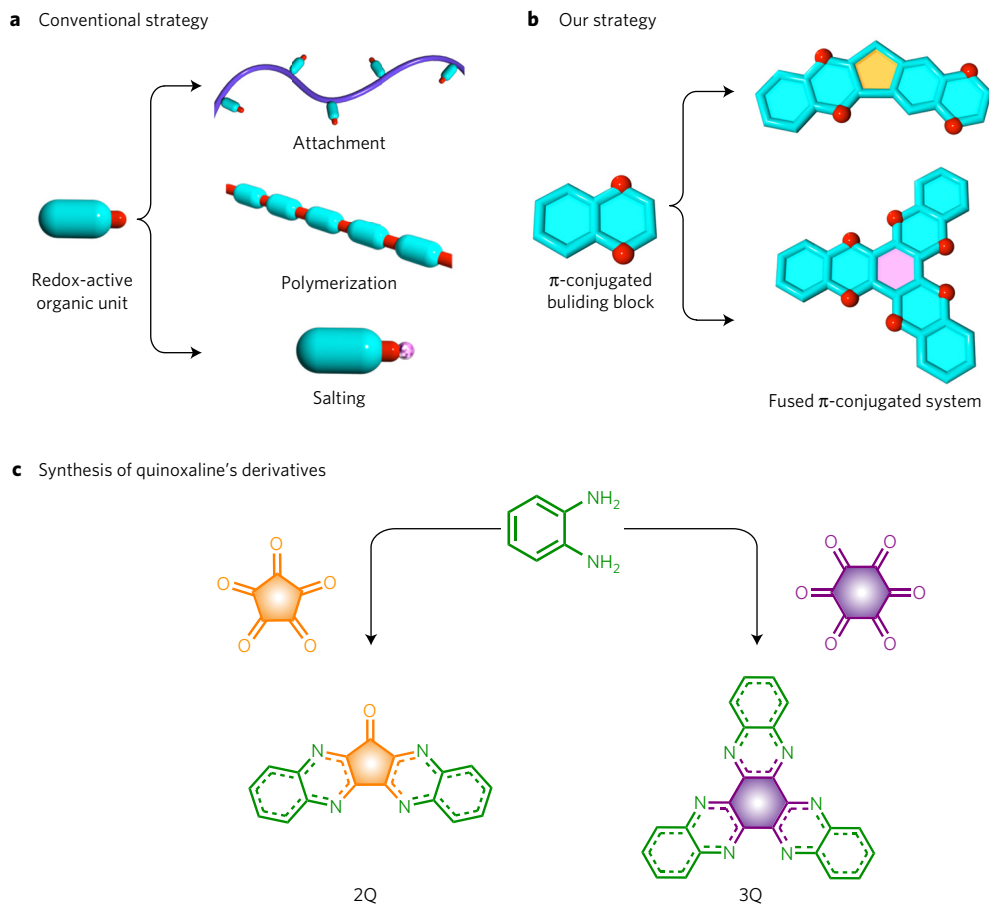


Figure 1 | Synthesis methods for redox organic molecules. **a**, Three conventional preparation routes: tethering polymers with redox groups, polymerization of organic redox groups and formation of organic salts. The molecular units and the electrochemically active sites are shown in cyan and red, and the polymer chains and the organic salts are marked by purple and pink, respectively. **b**, Our fusing strategy to synthesize extended π -conjugated heteroaromatic molecules. **c**, Synthetic scheme of quinoxaline's derivatives: diquinoxalinylene (2Q) and triquinoxalinylene (3Q) based on condensation reaction. The orange and purple parts represent five- and six-fused membered ring units, respectively.

pyrazine units in 3Q afford high-capacity lithium storage, and its extended π -conjugated system facilitates charge transport over the electrode. By mixing with graphene to form a conductive composite, the 3Q/graphene hybrid electrode exhibits a high capacity and long-term cycling stability. Nuclear magnetic resonance (NMR) studies are carried out to probe the redox reactions taking place in 3Q-based organic battery upon cycling. Taking advantage of the relatively high natural abundance (0.37%) and small spin moment ($I = 1/2$) of ^{15}N , we synthesize ^{15}N isotope-labelled 3Q, and analyse changes in its local environment by cross polarization/magic angle spinning (CP/MAS) solid-state NMR during lithiation/delithiation. A holistic approach combining NMR and density functional theory (DFT) studies is applied to elucidate the sequential structural evolution of 3Q during lithiation, allowing the lithiation dynamics at the aromatic pyrazine redox centre to be probed, thereby confirming that multi-electron transfer can be supported in 3Q.

Molecular engineering of quinoxaline's derivatives

The compounds diquinoxalinylene (2Q) or triquinoxalinylene (3Q) are synthesized via a condensation reaction between oxocarbons (C_nO_n , $n = 5$ (cyclopentanepentone) or $n = 6$ (cyclohexanehexone)) derived from biomass and *o*-phenylenediamine (see Methods and Fig. 1c). By bridging quinoxaline building blocks as electroactive sites and bypassing redox-inactive units, a high electron density per unit weight can be obtained, which in turn ensures a high specific capacity.

To evaluate the redox properties of these heteroaromatic molecules (Fig. 2a), the energy levels of the lowest unoccupied molecular orbital (LUMO) and the highest occupied molecular orbital (HOMO) are calculated using DFT. As shown in Fig. 2b, the LUMO of 2Q (-3.65 eV) and 3Q (-2.97 eV) are much lower than that of quinoxaline (-2.36 eV), indicating that 2Q and 3Q have greater electron affinities and higher reduction potentials as compared to quinoxaline. In addition, the gaps between the HOMO and LUMO levels are effectively reduced due to the extended π -electron orbital overlap in the conjugated molecules. As expected, the energy gaps (E_g) of 2Q (3.39 eV) and 3Q (3.66 eV) are much lower than that of quinoxaline (4.65 eV), suggesting that the intrinsic electronic conductivities in 2Q and 3Q are higher than for quinoxaline.

X-ray single crystallographic analysis reveals that 3Q crystallizes in a centrosymmetric monoclinic space group $P2(1)/c$, with lattice constants of $a = 19.3752(13)$ Å, $b = 5.3895(4)$ Å, $c = 20.8601(12)$ Å, $\beta = 104.157(3)^\circ$, volume = $2112.1(2)$ Å³ (Supplementary Table 1). The typical layered structure of 3Q, consisting of zig-zag and parallel-stacked structure held by π - π interactions and multiple hydrogen bonding, is given in Fig. 2c. Adjacent 3Q molecules that are arranged perpendicularly to each other interact through hydrogen bonding so that the distance between the H atom and the N atom ranges from 2.54 to 3.26 Å, and via CH/ π interactions with distances ranging from 2.89 to 3.34 Å. In addition, the adjacent parallel 3Q molecules are tightly packed through a displaced face-to-face π - π interaction and the distance between the N-fused heteroaromatic rings is 3.32 Å.

Electrochemical performance

The electrochemical properties are initially evaluated using coin-type cells assembled with metal lithium as the counter/reference electrode and crystalline 2Q and 3Q powders as the corresponding positive electrodes (see Methods). As shown in Fig. 3a, the galvanostatic charge/discharge curves of the 2Q display four pairs of slopes at about 3.1–2.6 V/2.7–2.5 V, 2.6–2.2 V/2.5–2.2 V, 2.2–1.7 V/2.2–1.8 V, 1.7–1.4 V/1.9–1.2 V, consistent with its cyclic voltammetry (CV) curves (Supplementary Fig. 1). The charge/discharge profile of a 3Q battery is shown in Fig. 3c, which exhibits two clear pairs of reversible plateaux at about 2.6–2.15 V/2.11–2.95 V and 1.68–1.38 V/1.41–1.75 V in the discharge/charge curves, corresponding to two reduction peaks during the cathodic CV scan (Supplementary Fig. 1). The CV characteristics of 2Q and 3Q clearly point to multiple redox reactions during the charging/discharging processes, and the highly reversible nature of these electrodes.

The battery performances of 2Q and 3Q are evaluated and the results show that these exhibit stable cycling performances (Fig. 3 and Supplementary Tables 2–4). Batteries using 2Q and 3Q can deliver an initial discharge capacity exceeding ~ 372 and 395 mAh g^{-1} under a current of 400 mA g^{-1} (1C) and retain ~ 359 and 324 mAh g^{-1} after 200 cycles, yielding a capacity retention of 96.4% and 82.1%, respectively (Supplementary Fig. 2). Furthermore, as the loading current is increased to 800 mA g^{-1} (2C), the specific capacities of 2Q and 3Q can reach ~ 300 and 318 mAh g^{-1} in the first cycle, which is gradually reduced to ~ 290 and 263 mAh g^{-1} after 200 cycles (Supplementary Fig. 2), resulting in a high-capacity retention of 96.7% and 82.5%, respectively. Even at large loading currents of 1.6 (4C) and 3.2 A g^{-1} (8C), the cycling performances of 2Q and 3Q show a remarkable stability over 1,000 cycles, with negligible capacity loss per cycle and a superior coulombic efficiency of nearly 100%, as shown in Fig. 3b,d.

The rate capabilities of 2Q and 3Q are also investigated. The 2Q battery shows stable reversible capacities of 373, 313, 272, 254, 241 and 236 mAh g^{-1} at current levels of 1C, 2C, 4C, 6C, 8C and 10C, respectively. Even at a high loading current of 20C, the 2Q battery can still render a capacity of 222 mAh g^{-1} , which corresponds to 60% of the initial specific capacity (Fig. 3e). For the 3Q battery, the corresponding values are 394, 334, 290, 268, 255 and 242 mAh g^{-1} at loading currents of 1C, 2C, 4C, 6C, 8C and 10C, respectively. More interestingly, a reversible capacity of 218 mAh g^{-1} is obtained at 20C (Fig. 3f), which attests to the facile charge exchange kinetics between the extended π -conjugated molecule and the lithium ions. Furthermore, the rate capability curves are highly reversible (no hysteresis) even when the cycles are carried out at different rates for both the organic electrodes.

In addition, the cycling performance of 2Q and 3Q are evaluated, and they deliver a reversible capacity of 229 and 215 mAh g^{-1} in the first cycle, respectively, while maintaining around 185 and 147 mAh g^{-1} after 10,000 cycles under a current of 20C, demonstrating a high-capacity retention of $\sim 70\%$ and 67%, respectively (Fig. 3g,h). Such high-capacity delivery and retention have not been observed so far in small-molecule-based battery systems. This result confirms that the strategy of fusing pyrazine-based building blocks to form extended π -conjugated compounds is highly effective for the fabrication of ultrafast, battery systems with highly stable performance.

The energy density and power density of 2Q and 3Q are calculated. Given that their initial capacity are about 373 – 394 mAh g^{-1} , and the average discharge potentials are 1.86–1.88 V, the energy densities of 2Q and 3Q are estimated to be $\sim 250 \text{ Wh kg}^{-1}$ (Supplementary Note 1 and Supplementary Fig. 3). This is much higher than the capacity (100 – 140 Wh kg^{-1}) of commercial Li-intercalation compounds such as LiCoO_2 , LiFePO_4 and LiMn_2O_4 . Even at a current loading of 20C (corresponding

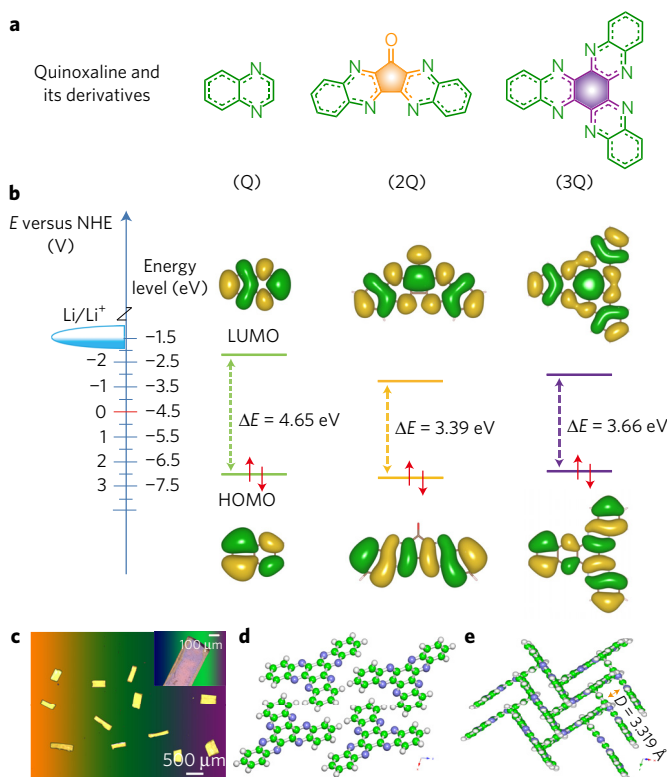


Figure 2 | Chemical structures and energy diagrams of quinoxaline and its derivatives. **a**, Chemical structures of quinoxaline and its derivatives, diquinoxalinylene (2Q) and triquinoxalinylene (3Q). **b**, Calculation of the relative energies and optimized structures of the molecules used in the study obtained using the DFT method with B3LYP/6–31+G(d, p) in DME solvent, the left axis represents the relative voltage (versus NHE) and the right axis represents the relative energy level in vacuum (E_{vac}).

c, Photograph image of crystals at $500 \mu\text{m}$ scale (inset, magnified image of one crystal at $100 \mu\text{m}$ scale). **d, e**, Single-crystal structure of triquinoxalinylene (3Q) shown as a ball-stick model (the green, blue and white balls represent carbon, nitrogen and hydrogen atoms, respectively).

to a full discharge within 3 min), 2Q and 3Q can still deliver capacities of $\sim 130 \text{ Wh kg}^{-1}$, affording a very high power density of $\sim 8 \text{ kW kg}^{-1}$ (Supplementary Note 1 and Supplementary Fig. 4). Nevertheless, the specific capacities decrease with an increase in active material loading due to the higher resistance of the organic material (Supplementary Figs 5–13 and Supplementary Note 2), and the volumetric energy density is at present unsatisfactory, which is common to all lightweight materials based on sulfur or organic compounds. However, the competitive electrochemical performance, along with the facile production process from natural precursors, is promising for large-scale battery applications.

Ex situ ^{15}N solid-state NMR on the 3Q electrode

To gain insight into the lithium storage mechanism of 3Q, we performed NMR studies in combination with DFT calculations to identify the structural changes associated with multiple electron transfer during battery operations (see Methods). Since three pairs of electroactive pyrazine N atoms in the 3Q molecule can strongly coordinate with lithium, we propose that six lithiated 3Q structures are formed during the discharge processes, including bidentate with single lithium ion (3Q-Li), bis-bidentate (3Q-2Li), tri-bidentate (3Q-3Li), tetra-bidentate (3Q-4Li), penta-bidentate (3Q-5Li) and hexa-bidentate (3Q-6Li) (Fig. 4a). Due to the different coordination patterns of nitrogen atoms and lithium ions in the 3Q molecule, the local electronic environment of the electroactive N is expected to

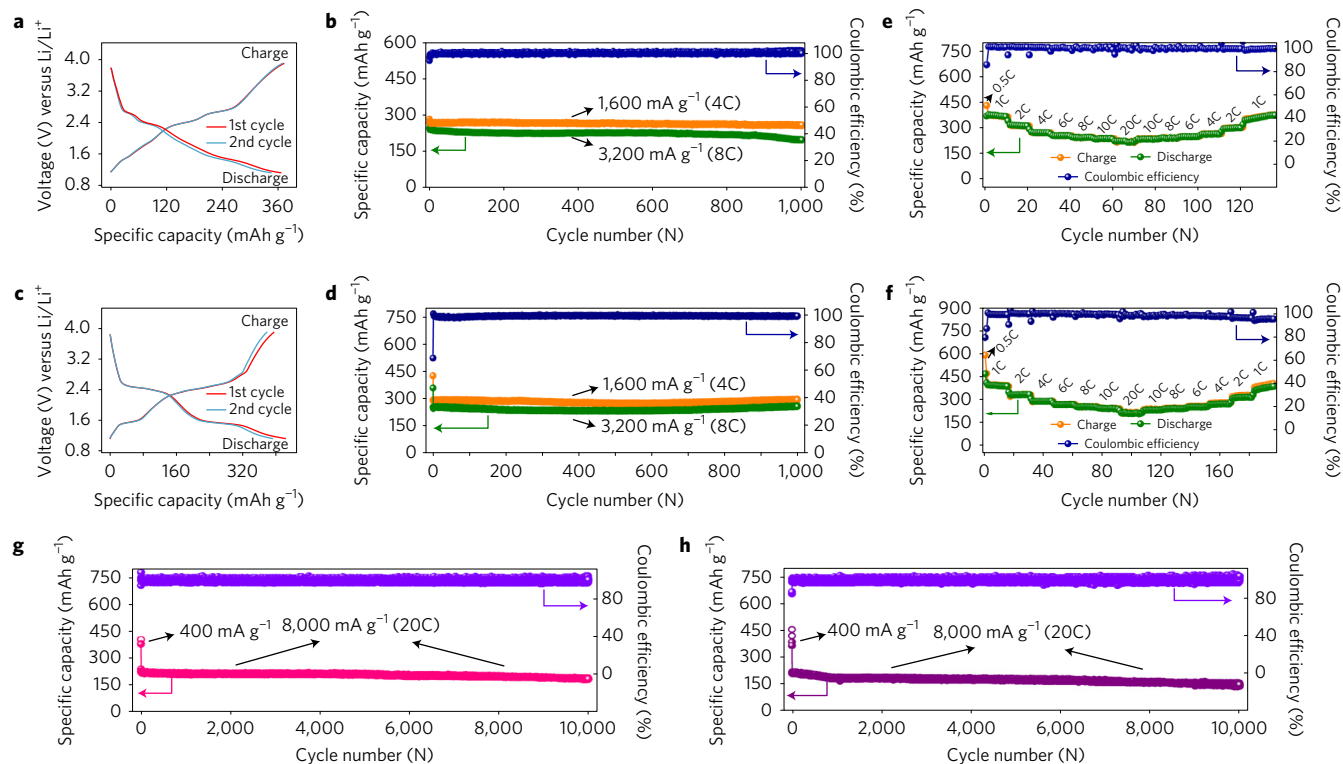


Figure 3 | Electrochemical characterization of the π -conjugated heteroaromatic compound based electrode. **a,c**, Capacity–voltage profile of 2Q and 3Q, respectively, at a current of 400 mA g^{-1} (1C). **b,d**, Cycling performance of 2Q and 3Q at a current of 1.6 A g^{-1} (4C) and 3.2 A g^{-1} (8C). **e,f**, Rate capabilities of 2Q and 3Q, respectively, at various current rates. **g,h**, Long-term cycling performances of 2Q and 3Q, respectively, under a current of 8 A g^{-1} (20C) for 10,000 cycles. The capacity retention of 2Q is $\sim 86\%$, $\sim 81\%$ and $\sim 70\%$ after 2,000, 6,000 and 10,000 cycles, respectively. The capacity retention of 3Q is $\sim 82\%$, $\sim 80\%$ and $\sim 65\%$ after 2,000, 6,000 and 10,000 cycles, respectively.

change dynamically during the lithiation and delithiation processes. It can be predicted that five different ^{15}N resonances might be observed, namely, N1 (the signal assigned to pristine 3Q without binding to Li), N2 (the signal due to the non-bonded pyrazine N situated furthest away from Li), N3 (the signal due to the non-bonded pyrazine N nearest to a co-shared Li-bonded bipyridine-type site), N4 (the signal due to the co-shared one-Li-bonded pyrazine N), and N5 (the signal due to the co-shared two-Li-bonded pyrazine N).

To elucidate the structural evolution during the battery process, we labelled 3Q with ^{15}N and performed *ex situ* solid-state NMR to monitor the variation of ^{15}N resonances at various potentials during the cycling processes. As shown in Fig. 4b–d and Supplementary Fig. 14, in the initial stage, ^{15}N -labelled pristine 3Q sample exhibits one strong singlet centred at $\delta = -55$ ppm, which is assigned to the six equivalent nitrogen atoms (N1) in 3Q. When the 3Q/Li cell is initially discharged to 2.4 V, three distinct N resonances at $\delta = -66.8$, -87 and -239.8 ppm emerge besides the original one at -55 ppm, corresponding to N2, N3 and N4, respectively. The appearance of three different chemical environments of N indicates that 3Q coordinates with one lithium ion to form 3Q-Li (Fig. 4c). At this stage, a radical species is generated and an unpaired electron is delocalized between the two bidentate N atoms, as confirmed by electron spin resonance (ESR) spectra (Supplementary Fig. 15). After discharging to 2.0 V, N2, N3 and N4 peaks at $\delta = -65.5$, -86.7 and -236.3 ppm remain, while N4 increases, implying the formation of 3Q-2Li. When the 3Q/Li cell is further discharged to 1.82 V, the N4 peak increases in intensity, suggesting the parallel emergence of 3Q-3Li. The presence of N1, N2 and N3 peaks indicates incomplete conversion due to the kinetic limitations in the solid-state electrochemical reaction. As the 3Q/Li cell is discharged to 1.7 V, the N4 peak decreases in relative intensity and

a new N5 peak at $\delta = -297$ ppm appears, indicating the structural conversion to 3Q-4Li due to the two nitrogen atoms coordinating with two lithium ions. With further discharge, the N5 resonance at $\delta = -301.5$ ppm increases strongly in intensity, while a much weakened N4 peak remains, suggesting the formation of a 3Q-5Li type compound in the subsequent lithiation step. Discharging further, the N5 resonance at $\delta = -302$ ppm grows, but the N4 resonance becomes weaker and disappears, revealing a conversion to 3Q-6Li. During delithiation, when the 3Q/Li cell is charged to 1.72 V, the N4 peak at $\delta = -238$ ppm increases, indicating the formation of 3Q-5Li. When the voltage reaches 2.5 V, the N2 and N3 resonances grow at the expense of the N5 peak, confirming the recovery of 3Q-2Li and 3Q-3Li (Supplementary Fig. 16). At the end of charging, the N1 signal returns to the original position, demonstrating the recovery of 3Q and the reversible nature of the lithiation reactions.

Similarly, in the initial stage, pristine 3Q shows three ^{13}C resonances at ~ 126 (C1), ~ 133 (C2) and ~ 140 ppm (C3) (Fig. 4d). When 3Q is discharged to 1.12 V, a new signal at ~ 120 ppm (C4) appears, suggesting increased lithium coordination and a loss of aromaticity in the π -conjugated lithiated 3Q during the discharge processes. At the end of the charge state, ^{13}C resonances return to the initial chemical shift, confirming the reversible nature of the electrochemical reactions of 3Q during the charging/discharging processes.

The structural reversibility of 3Q is monitored in the subsequent cycling. The colour-mapped ^{15}N and ^{13}C NMR spectra taken at various stages during the first and second cycle along with the corresponding voltage–capacity curves are shown in Fig. 4e–g. In the initial stage, one strong singlet centred at $\delta = -55$ ppm (N1), which is assigned to pristine 3Q sample, evolves, while new peaks at ~ -88 (N2), -235 (N3) and -300 ppm (N4) emerge during cycling; these peaks vanish and the original peak at -55 ppm (N1)

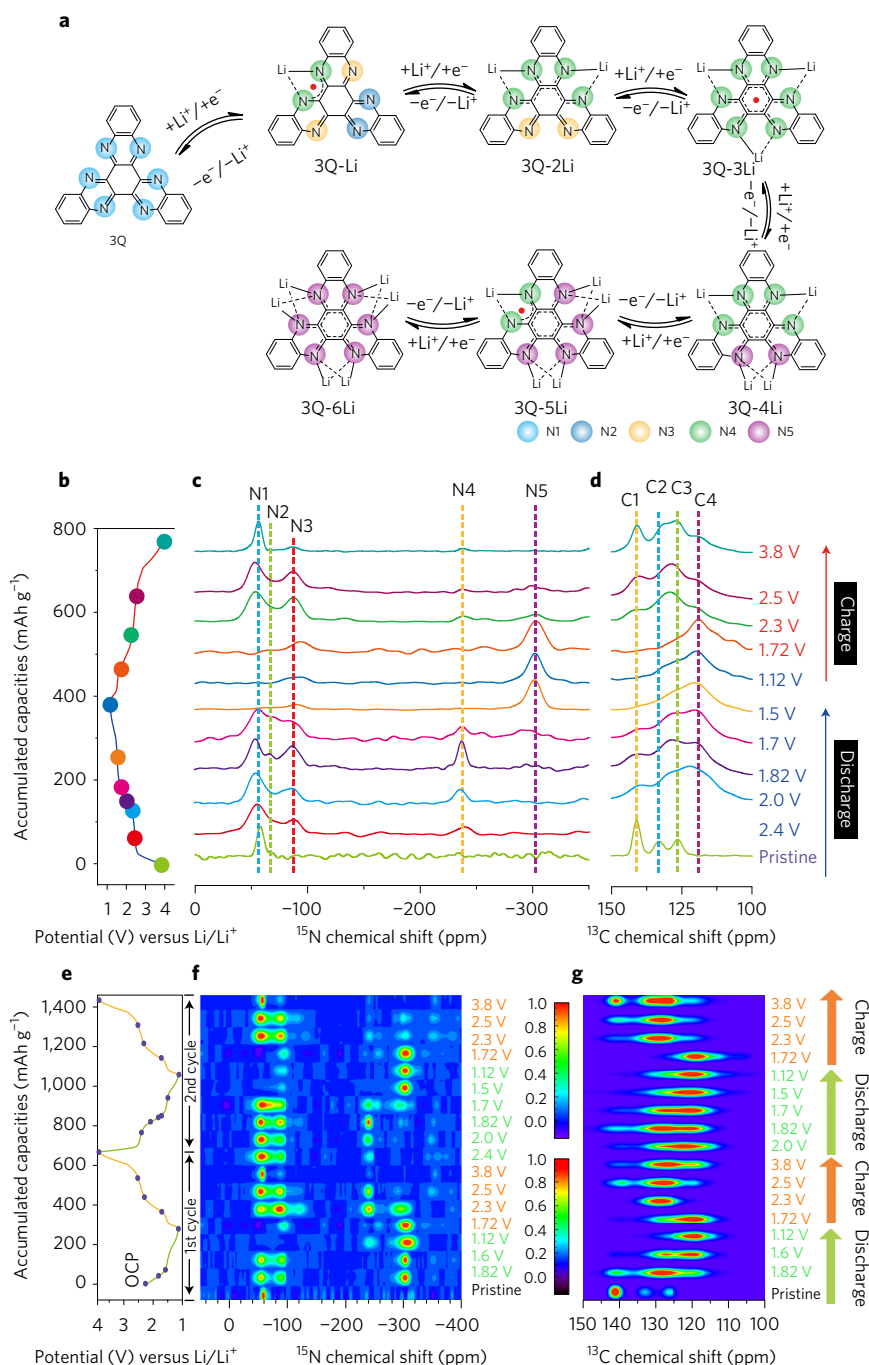


Figure 4 | Structural evolution during charge/discharge. **a**, The predicted lithiated structures of 3Q during the discharging process. Different colours are used to distinguish N atoms in different chemical environments. (The same colour scheme is used for plots with similar chemical shifts in NMR. For example, 3Q-Li and 3Q-2Li share the same chemical shifts based on the coordination of two N atoms with one Li.) **b**, The galvanostatic charge/discharge profile of 3Q/Li cycled at a rate of C/20 during the second cycle. **c,d**, *Ex situ* ¹⁵N and ¹³C solid-state NMR spectra, respectively, of the electrode materials cycled to different charge states, as marked on the corresponding electrochemical profiles. N1, N2, N3, N4 and N5 represent the different NMR chemical shifts in ¹⁵N spectra involving the labelled lithiated/delithiated samples during the charge/discharge processes. C1, C2, C3 and C4 are the different NMR chemical shifts in ¹³C spectra involving lithiated/delithiated samples. **e**, The galvanostatic charge/discharge profile of 3Q/Li cycled at a rate of C/20 during the first and second cycles. **f,g**, The colour-mapped profile for ¹⁵N and ¹³C solid-state NMR spectra, respectively, of the electrode materials cycled to different charge/discharge states during the first and second cycles.

recovers during the charging process. In parallel, three ¹³C NMR peaks appear initially at ~140, 133 and 126 ppm; these peaks evolve with discharge, where a new peak is seen at ~120 ppm. Finally, the ¹³C NMR spectra recover to the initial peak position at the end of the discharge process. The evolution of the ¹⁵N and ¹³C NMR peak positions show a similar trend during the discharging/charging

processes of the first and second cycle, which demonstrates the highly reversible nature of both the redox reactions as well as the concomitant structural changes of the 3Q electrode material.

A schematic overview of the various structural changes taking place during the lithiation of 3Q based on results from the solid-state NMR experiments is shown in Supplementary Fig. 17. When

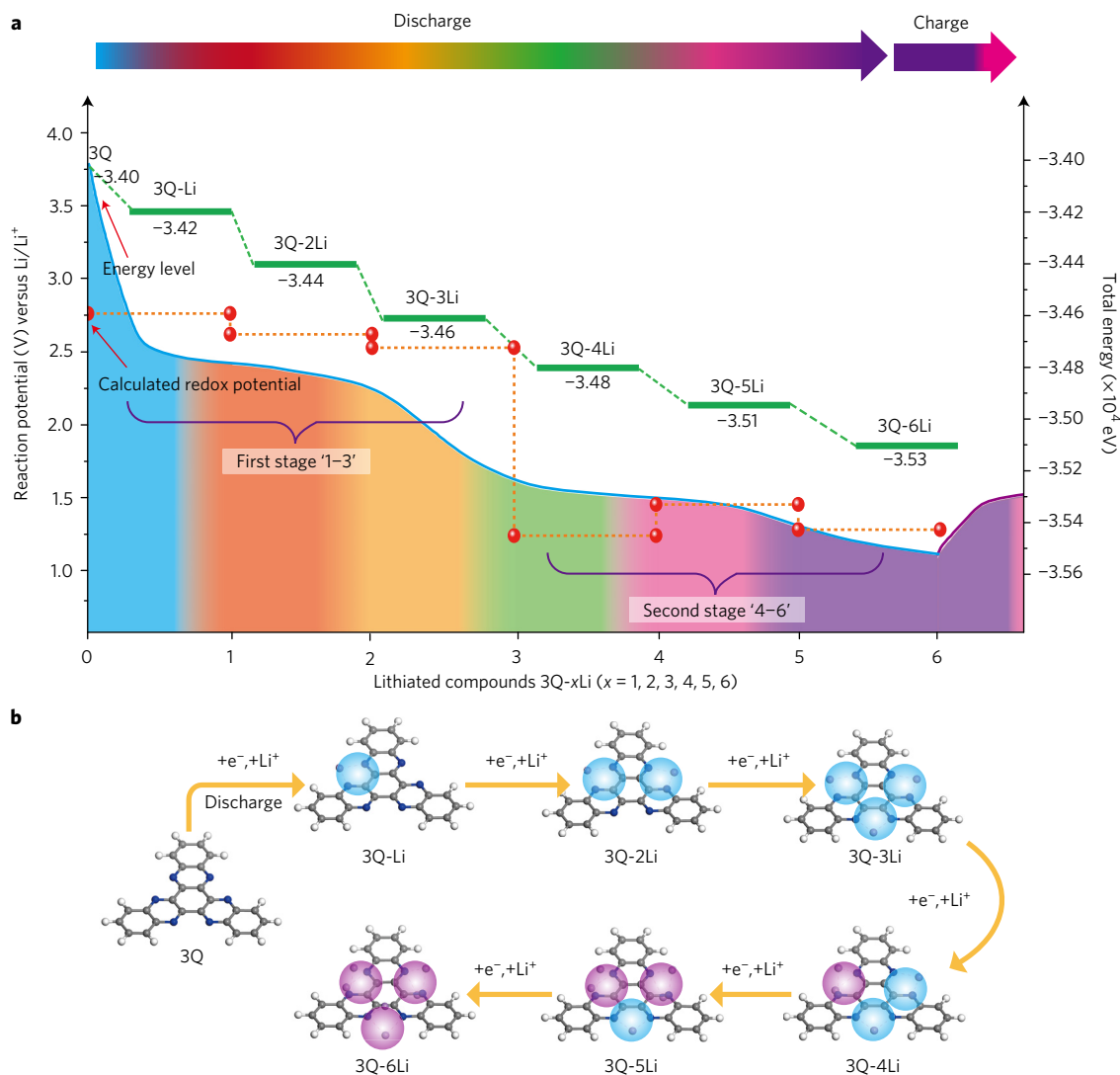


Figure 5 | The lithiation pathway obtained from simulations. a, The left axis shows the redox potential versus Li^+/Li where the calculated potentials are marked by dotted red lines. The right axis shows the total energy (eV) of various lithiated 3Q structures, which is defined by the sum of the electronic and zero-point energies. The energies of the most stable structure at each lithiated stage are marked by green lines. The discharge curve is marked by the blue line, and the shaded and coloured areas indicate the evolution of various lithiated 3Q structures. **b**, The structure evolution during the lithiation. The binding sites between lithium and bipyridine are indicated by blue and purple balls, which represent five-membered ring structures and pseudo-tetrahedral structures, respectively.

the cell is discharged to 1.2 V, the six lithiated structures evolve from 3Q to 3Q-xLi ($x = 1, 2, 3, 4, 5, 6$) in a highly reversible way, implying efficient six electron transfer per molecule during the lithiation, which contributes to the high lithium uptake capacities observed experimentally.

DFT simulation of the lithiated 3Q

To further understand the redox energies of transformation of 3Q accompanying the multiple lithiation processes, we applied DFT to simulate the lithiation processes of 3Q. The optimized structures of 3Q-xLi ($x = 0, 1, 2, 3, 4, 5, 6$) and their total energies, defined by the sum of electronic and zero-point energies, are shown in Supplementary Fig. 18 and Supplementary Table 5, respectively. The structural evolutions of 3Q along the lithiation pathway are in accordance with the evidence from the ^{15}N NMR results (see Methods and Supplementary Figs 19 and 20). In addition, we note that 3Q-Li, 3Q-3Li and 3Q-5Li are in a doublet state. To examine how the unpaired electron or radical delocalizes within the π -conjugated system, the Mulliken atomic spin densities of 3Q-xLi

($x = 1, 3, 5$) are calculated (Supplementary Fig. 21). It is found that the majority of the spin densities are distributed on the co-shared one-Li-bonded pyrazine nitrogen in the extended π -conjugated planar rings of 3Q-Li, 3Q-3Li and 3Q-5Li. The results of spin distribution on the equivalent pyrazine nitrogen are in accordance with the proposed lithiation mechanism as shown in Fig. 4a.

To investigate the redox potential of 3Q upon lithiation, we calculate the sum of the electronic and thermal Gibbs free energies of the optimized 3Q-xLi structures (Supplementary Table 6). It is found that the redox energies for the first three redox couples (namely, $3\text{Q}/3\text{Q-Li}$, $3\text{Q-Li}/3\text{Q-2Li}$ and $3\text{Q-2Li}/3\text{Q-3Li}$) are within 0.25 V of each other, while those for the next three redox couples ($3\text{Q-3Li}/3\text{Q-4Li}$, $3\text{Q-4Li}/3\text{Q-5Li}$ and $3\text{Q-5Li}/3\text{Q-6Li}$) are within 0.22 V of each other. This implies the existence of two main redox energy levels, in agreement with the two broad peaks observed in the CV curves (Supplementary Fig. 1). The reaction potentials for the six redox couples are calculated and the calculated redox plateau is highlighted in Fig. 5, which shows the two redox potential levels. This means that the redox reactions of 3Q manifest as two three-

electron processes, which can be highly feasible due to the closely spaced energy levels. Compared with the discharge curve in Fig. 5, the calculated potentials also reveal two main discharge plateaux at around 2.6–2.15 V (labelled as ‘1-2-3’) and 1.68–1.38 V (labelled as ‘4-5-6’), in accordance with the two-step three-electron transfer mechanism. The slight slope at the end of each stage is due to the slow redox kinetics of the solid-state redox reaction involving the organic electrode, corresponding to the third-electron reaction for each stage. Finally, the sharp drop in potential between the two discharge plateaux observed in the experiment can be rationalized from binding energy considerations. The average binding energies for the first three-lithium reaction is about -2.9 eV, while that for the last three-lithium reaction is about -1.7 eV. Starting from the fourth lithium reaction, the binding energy reduces by about 40% (Supplementary Table 5). This is attributed to the fact that lithium binding is stronger when two nitrogens are bonded to one lithium (the first three lithiation stages) while the binding strength is drastically reduced when two nitrogen atoms are bonded to two lithiums, which is the case in the last three lithiation stages.

Conclusions

In summary, we have demonstrated that π -conjugated heteroaromatic molecules can be used as solid-state organic cathode and the latter exhibits high specific capacity as well as excellent cycle stability in rechargeable lithium-ion batteries. The heteroaromatic molecules are made from fused quinoxaline building blocks, which afford multiple redox-active sites and improve stability in electrolyte. In addition, hybridizing the molecules with graphene, and using an ether-based electrolyte to form an effective solid electrolyte interphase (SEI), allows the organic electrode to exhibit high capacity and long-cycle life. *Ex situ* NMR studies correlate the high capacity of 3Q to the presence of multiple sites for lithiation on the pyrazine nitrogen atoms in the quinoxaline building block. Corresponding to the six pyrazine nitrogen atoms in 3Q, six lithiated/delithiated intermediates evolve during the highly facile six electron-transfer reactions and contribute to the high capacity of 3Q. Our multifaceted approach is expected to pave the way towards the development of small-organic-molecule-based cathode materials for lithium ion batteries with superior energy density and long lifespan.

Methods

Synthesis of triquinoxalinylene. Triquinoxalinylene (3Q) is synthesized according to a previous report with some modifications (Fig. 1c)⁴⁰. Specifically, hexaketocyclohexane (0.499 g, 1.6 mmol, Aldrich) is dissolved in acetic acid (AcOH)/ethanol (1:1 in vol./vol., 25 ml) under stirring, to which *o*-phenylenediamine (0.53 g, 4.8 mmol, Aldrich) is added. After flushing with Ar for 15 min, the solution is heated under reflux for 24 h. The dark green suspension is filtered and washed successively with hot acetic acid, acetone, water and ethanol. The resulting dry dark green suspension is boiled with 50 ml 30 wt% HNO₃ at 140 °C for 3 h under stirring. Finally, the brown suspension is filtered and the filter cake is washed well with deionized water and ethanol, and dried in vacuum to form a yellow-orange solid (~350 mg, yield 57%). ¹H NMR (500 MHz, CF₃COOD, 300 K): δ (ppm) 8.71 (m, 6H), 8.37 (m, 6H); ¹³C NMR (125 MHz, CF₃COOD, 300 K): δ (ppm) 143.7, 140.6, 139.8 and 130.0. (Supplementary Figs 22 and 23). Elemental analysis: calculated for C₂₄H₁₂N₆: C, 74.99; H, 3.15; N, 21.86%; found: C, 74.10; H, 2.96; N, 22.08%. ESI-MS *m/z* calculated for C₂₄H₁₂N₆: 385.1 [M+H]⁺; found: 385.4. FT-IR (KBr): 3,447 (m), 1,493 (s), 1,364 (s), 1,338 (s), 1,077 (s), 768 (s), 756 (s), 608 cm⁻¹ (m) (Supplementary Fig. 24). Furthermore, single-crystalline 3Q can be obtained through slow evaporation of its saturated solution in chloroform/trifluoroacetic acid solvent (4:1 in vol.) (See Supplementary Note 3 and Fig. 25).

Synthesis of leuconic acid. Leuconic acid is synthesized according to a previous report⁴¹. Concentrated nitric acid (30 ml, 60 wt%) is added into a flask and cooled to 0 °C using an ice-bath. 3.92 g (20 mmol) croconic acid trihydrate is added gradually into the flask over 10 min. The mixture is cooled and kept stirring under a slow stream of flowing air until it turns colourless and nitrogen oxide fumes evolution has stopped. An equal volume of previously cooled methanol is added while stirring. The resulting white solid is collected by vacuum filtration, washed with 60 ml of cold methanol, and dried in a vacuum desiccator.

The resulting compound is further purified by recrystallization in a 1:1 mixture of ethanol and isopropanol. The titled compound is obtained as colourless solid (~3.5 g, yield 75%) and used without purification.

Synthesis of diquinoxalinylene. Diquinoxalinylene (2Q) is synthesized using a similar procedure to that for 3Q, except for using leuconic acid instead of hexaketocyclohexane (Fig. 1c). ¹H NMR (500 MHz, CDCl₃, 300 K): δ (ppm) 8.40 (m, 4H), 7.97 (m, 4H); ¹³C NMR (125 MHz, CDCl₃, 300 K): δ (ppm) 187.3, 153.6, 149.1, 144.6, 144.0, 133.9, 132.4, 131.9 and 130.8. (Supplementary Figs 26 and 27) Elemental analysis: calculated for C₁₇H₈N₄O: C, 71.83; H, 2.84; N, 19.71%; found: C, 71.67; H, 2.56; N, 19.44%. ESI-MS *m/z* calcd for C₁₇H₈N₄O: 285.1 [M+H]⁺; found: 285.2. FT-IR (KBr): 3,458 (m), 1,738 (s, CO st), 1,545 (s), 1,500 (s), 1,358 (s), 1,073 (s), 785 (m), 762 cm⁻¹ (m).

Electrochemical measurements. The electrochemical properties and galvanostatic charge/discharge are evaluated in a 2016-type coin cell with a lithium chip as the counter electrode, a glass microfibre membrane (Whatman GF/D, Aldrich) as the separator, and 1.0 mol l⁻¹ LiTFSI-DOL/DME solution (Solvionic) as the electrolyte. The working electrode is composed of a mixture containing 30 wt% of active materials: namely, diquinoxalinylene (2Q) or triquinoxalinylene (3Q), 60 wt% graphene, and 10 wt% (poly(vinylidene fluoride)) PVDF binder. The composites are first dispersed in *N*-methyl-2-pyrrolidone (NMP) to form a slurry and cast on an aluminium foil by doctor blading. The electrode is dried at 80 °C overnight in a vacuum oven and punched into circular electrodes before the assembly of the cell. All the cells are assembled in a glove box with [O₂], [H₂O] \leq 1 ppm. The galvanostatic charge/discharge tests at different current densities are performed on a LAND cyler (Wuhan Kingnuo Electronic) at ambient temperature. The lithium uptake capabilities of the organic electrodes are calculated based on the active materials of 2Q and 3Q and by deducting the capacity contribution from graphene. The cut-off voltage is set to above 1.2 V, the delivered capacity of graphene is estimated to be ~49 mAh g⁻¹ at a current of 400 mA g⁻¹ (1C) (Supplementary Fig. 28). Cyclic voltammetry measurements are carried out in the voltage range of 1.2–3.9 V at a scan rate of 0.1 mV s⁻¹ using IVIUM electrochemical instrumentation (IVIUM Technologies).

***Ex situ* ¹⁵N MAS NMR spectroscopy.** To obtain a high-sensitivity, high-resolution solid-state NMR signal, ¹⁵N isotope-labelled samples are used. Before the experiment, ¹⁵N-labelled triquinoxalinylene (3Q) is prepared using a similar procedure as above for 3Q through a condensation reaction between oxocarbons and ¹⁵N-labelled *o*-phenylenediamines (mol. wt.:110.13, purity: \geq 99 wt%, Toronto Research Chemicals). In addition, to enhance the output signal for the chemical shifts in the ¹⁵N-labelled samples, prototype pouch cells (shown in Supplementary Fig. 29) are designed to obtain a sufficient quantity of labelled samples. A mixture composed of 60 wt% the organic active material, 30 wt% conductive graphene and 10 wt% PVDF binder is stirred in NMP to make a slurry, which is pasted on one side of an aluminium foil (typical size 50 mm \times 100 mm) using a micrometer-adjustable film applicator (50 mm-EQ-Se-KTQ-50, MTI). The films (mass loading of electrode material ~35 mg) are dried at 80 °C overnight under vacuum and used as the cathode, a metal Li ribbon (typical size 55 \times 110 mm, thickness 0.58 mm) is used as the counter electrode, and a glass microfibre membrane (Whatman GF/D, Aldrich) is used as the separator. All the cell components are assembled in a laminated aluminium bag filled with 1.0 mol l⁻¹ LiTFSI-DOL/DME solution electrolyte in an Ar-filled glovebox and sealed. After storing overnight for equilibration, the pouch cells are cycled galvanostatically at a current density of C/20 to various target voltages in the range 1.2–3.9 V and calibrated to equilibrium state at the target voltages until the current falls to below C/60 (2.4, 2.0, 1.82, 1.7, 1.5, 1.2 V during the lithiated stage, and 1.7, 2.3, 2.5, 3.8 V during the delithiated stage) for *ex situ* NMR measurements. Samples at various lithiated/delithiated stages are prepared by disassembling the pouch cells in an Ar-filled glovebox followed by rinsing the electrodes with dimethyl carbonate and drying in vacuum; the samples for NMR measurements are obtained by scratching the electrode and packed in the MAS rotor (diameter 4 mm) in glove box. Solid-state CP/MAS ¹⁵N NMR spectra are recorded on a Bruker Avance III spectrometer at 40.5 MHz under a spinning rate of 12 kHz using a p/2-(one-pulse) and/or a Hahn-echo (p/2-t-p-t) sequence. All the ¹⁵N NMR chemical shifts are referenced to neat nitromethane (at 0 ppm) as the external reference.

Density functional theory simulation. Geometry optimizations are performed without symmetry restriction using the B3LYP hybrid density functional^{42,43} implemented in Gaussian 09 suite of program⁴⁴. The 6-31+G(d,p) basis sets⁴⁵⁻⁴⁷ are adopted for H, Li, C, N and O atoms. ‘Tight’ optimization and ‘ultrafine’ integration grid are specified for the DFT calculations. The program’s default threshold values for self-consistency-field energy, total energy and force are adopted. 1, 2-dimethoxyethane (DME) is used as the solvent within the polarization continuum model (PCM)⁴⁸. Four parameters are set for this solvent: the static dielectric constant (ϵ) = 7.20; the molecular radius of the

solvent = 2.78255 Å; the density of the solvent = 0.005804 particles Å⁻¹ and the molar volume of the solvent = 103.7911 cm⁻³. The rest of the solvent parameters are based on a solvent having similar dielectric constant as DME ($\epsilon = 7.2273$, dibromomethane). We have checked that using the rest of the solvent parameters of another solvent such as water ($\epsilon = 78.3553$, the default solvent in the program) gives numerically the same results, indicating the solvent results in this work are mainly controlled by the above-mentioned four parameters. The thermal correction to Gibbs free energy is obtained from vibrational frequency calculations in the solvent. No negative frequency is found in any of the optimized structures. The redox potential (E_{redox}°) of the lithiation process (in volts) is calculated using the formula:

$$E_{\text{redox}}^{\circ} = -(G_f^{\circ} - G_i^{\circ} - G_{\text{Li}}^{\circ})/nF \quad (1)$$

where G_f° , G_i° and G_{Li}° are sum of electronic and thermal Gibbs free energy of the final and initial lithiated states of the organic molecule, and lithium atom (in kcal per mole); n is the number of electrons in the lithiation process, and F is the Faraday constant (which is 23,061 kcal per volt–mole). The binding energy (ΔE , in hartree units) of the lithiated molecules is calculated using the formula:

$$\Delta E = E_{m\text{Li}} - (E_{(m-1)\text{Li}} + E_{\text{Li}(0)}) \quad (2)$$

where m is the number of lithium atoms, and $E_{m\text{Li}}$, $E_{(m-1)\text{Li}}$ and $E_{\text{Li}(0)}$ denote the sum of electronic and zero-point energies for a lithiated molecule with m lithium atoms, with $m - 1$ lithium atoms and for the lithium atom, respectively. The negative energy of the molecule indicates that the binding is exothermic. The more negative the value, the stronger the binding between the lithium atom and the molecule.

Morphology characterization and analysis. The morphology of 3Q after cycling it in 2016-type coin cells to different cycle numbers (that is, 10, 500, 2,000, 5,000 cycles), followed by holding at its delithiated state for more than 6 h to extract residual Li, is characterized by high-resolution TEM. Prior to TEM imaging, the cells are disassembled in an Ar-filled glovebox, rinsed with dimethyl carbonate (DMC) and dried in the transfer chamber under vacuum, after which samples are collected and dispersed in DMC solvent. For synchrotron radiation photoemission spectroscopy (SRPES) analysis, the electrodes in 2016-type coin cells are charged and discharged to 1,000 cycles, following which the cells are disassembled in the Ar-filled glovebox, washed with DMC and dried under vacuum. The dry electrodes are fixed on a holder with adhesive tape and wrapped hermetically with Mylar film. SRPES measurements are carried out at the SINS (Surface, Interface and Nanostructure Science) beamline of SSSL (Singapore Synchrotron Light Source (SSLS), Singapore). All the samples are measured at room temperature in a ultrahigh vacuum chamber with a base pressure of 1×10^{-10} mbar. We calibrated the photon energy using the Au 4f7/2 core level peak at 84.0 eV of a sputter-cleaned gold foil in electrical contact with the sample. To obtain a large cross-section and high surface sensitivity, we used an 800 eV photon energy to probe the spectra of C_{1s}, N_{1s}, O_{1s}, F_{1s}, and a 400 eV photon energy to probe the spectra of Li_{1s}, C_{1s}, S_{2p}. All the UPS spectra are referenced to the Fermi edge of Au and all the PES spectra are normalized.

The changes in the morphology of the SEI formed on the surface of the organic electrode material have been monitored by high-resolution TEM images. As shown in Supplementary Fig. 30a–d, an amorphous layer is deposited on the organic electrode material during the battery operation. The inner core consists of fibre-like structures of 3Q (Supplementary Fig. 31), while the outer surface is made of a robust SEI layer. Further investigation reveals that the SEI develops a uniform thickness of ~10 nm after 500 cycles (Supplementary Fig. 32). The growth of a compact SEI layer on the surface of 3Q protects it from dissolution and improves its stability during cycling. In contrast, no distinct SEI layer is observed on the surfaces of organic electrode materials after cycling in a conventional electrolyte such as LiPF₆-EC/DMC (Supplementary Fig. 33), where a severe decay in the capacity during cycling is observed (Supplementary Fig. 34).

SRPES is used to elucidate the chemical compositions of the SEI layer formed on the surface of the electrode material after cycling in the ether-based electrolyte composed of 1M LiTFSI-DOL/DME. Supplementary Fig. 30e–j displays the high-resolution N_{1s}, F_{1s}, Li_{1s}, S_{2p}, C_{1s} and O_{1s} XPS spectra derived from the electrode materials after cycling. Compared with the XPS spectra of organic electrode before cycling (shown in Supplementary Fig. 35), the N_{1s} peak at about 396.4 eV for the as-prepared electrode is replaced by a new peak at 400.2 eV which is assignable to the formation of Li–N= species⁴⁹. In addition, the F_{1s} peak arising from C–F bonds in the PVDF binder at about 688.3 eV decreases after cycling⁵⁰. A strong peak evolves at about 685.6 eV instead, coupling with the Li_{1s} peak at 56.2 eV, suggest the formation of a dense LiF-rich SEI⁵¹. The emergence of S_{1s} spectra at 163.8 eV, following by peaks at 164.9 and 169.3 eV, suggests the presence of sulfate-, sulfite- and sulfide-based species (for example, Li₂S, Li₂S₂O₄, Li₂SO₃, Li₂SO₄) in the SEI^{52,53}. Compared with the electrode before cycling, the

appearance of chemically shifted components at the higher binding energy side for the C_{1s} and O_{1s} peaks suggests the formation of oxygen-based compounds (that is, CH₃CH₂COOLi, CH₃CH₂OLi, CH₃OLi, HCH₂OLi, poly-DOL oligomers, and so on) in the SEI⁵⁴. To further detect the compositions in different depths, the organic electrode material is also studied by means of a synchrotron radiation soft X-ray source with an energy of 400.0 eV (Supplementary Fig. 36). A new C_{1s} peak appears at 292.6 eV in addition to the above carbon peaks, which could be assigned to –CF₃ species from LiTFSI or their reaction products from the organic material, revealing abundant residual lithium salts mixing in the outer part of the solid interface film⁵⁵. High-resolution TEM and SRPES analysis confirm that the SEI film is made of a composite of a robust inorganic material and an elastic organic material formed during the decomposition of the ether-based electrolyte^{56,57}. It can be inferred that the inorganic components provide mechanical stability to support the structure of the SEI and the organic components provide lithium ion transport. This synergistic effect leads to the long-term stable cycling performance of the rechargeable organic battery.

Data availability. The data that support the plots within this paper and other findings of this study are available from the corresponding author upon reasonable request.

Received 16 October 2016; accepted 6 April 2017;
published 8 May 2017

References

- Larcher, D. & Tarascon, J.-M. Towards greener and more sustainable batteries for electrical energy storage. *Nat. Chem.* **7**, 19–29 (2015).
- Armand, M. *et al.* Conjugated dicarboxylate anodes for Li-ion batteries. *Nat. Mater.* **8**, 120–125 (2009).
- Morita, Y. *et al.* Organic tailored batteries materials using stable open-shell molecules with degenerate frontier orbitals. *Nat. Mater.* **10**, 947–951 (2011).
- Nokami, T. *et al.* Polymer-bound pyrene-4, 5, 9, 10-tetraone for fast-charge and -discharge lithium-ion batteries with high capacity. *J. Am. Chem. Soc.* **134**, 19694–19700 (2012).
- Hong, J. *et al.* Biologically inspired pteridine redox centres for rechargeable batteries. *Nat. Commun.* **5**, 5335 (2014).
- Song, Z., Zhan, H. & Zhou, Y. Polyimides: promising energy-storage materials. *Angew. Chem. Int. Ed.* **49**, 8444–8448 (2010).
- Huang, W. *et al.* Quasi-solid-state rechargeable lithium-ion batteries with a calix[4]quinone cathode and gel polymer electrolyte. *Angew. Chem. Int. Ed.* **52**, 9162–9166 (2013).
- Zhu, Z. *et al.* All-solid-state lithium organic battery with composite polymer electrolyte and pillar[5]quinone cathode. *J. Am. Chem. Soc.* **136**, 16461–16464 (2014).
- Deng, W. *et al.* A low cost, all-organic Na-ion battery based on polymeric cathode and anode. *Sci. Rep.* **3**, 2671 (2013).
- Zhao, L. *et al.* Disodium terephthalate (Na₂C₈H₄O₄) as high performance anode material for low-cost room-temperature sodium-ion battery. *Adv. Energy Mater.* **2**, 962–965 (2012).
- Kim, Y. J., Wu, W., Chun, S.-E., Whitacre, J. F. & Bettinger, C. J. Catechol-mediated reversible binding of multivalent cations in eumelanin half-cells. *Adv. Mater.* **26**, 6572–6579 (2014).
- Reed, L. D., Ortiz, S. N., Xiong, M. & Menke, E. J. A rechargeable aluminum-ion battery utilizing a copper hexacyanoferrate cathode in an organic electrolyte. *Chem. Commun.* **51**, 14397–14400 (2015).
- Häupler, B. *et al.* Aqueous zinc-organic polymer battery with a high rate performance and long lifetime. *NPG Asia Mater.* **8**, e283 (2016).
- Gan, S., Zhong, L., Gao, L., Han, D. & Niu, L. Electrochemically driven surface-confined acid/base reaction for an ultrafast H⁺ supercapacitor. *J. Am. Chem. Soc.* **138**, 1490–1493 (2016).
- Vlad, A., Singh, N., Rolland, J., Melinte, S., Ajayan, P. M. & Gohy, J.-F. Hybrid supercapacitor-battery materials for fast electrochemical charge storage. *Sci. Rep.* **4**, 4315 (2014).
- Suga, T., Konishi, H. & Nishide, H. Photocrosslinked nitroxide polymer cathode-active materials for application in an organic-based paper battery. *Chem. Commun.* **2007**, 1730–1732 (2007).
- Choi, W., Harada, D., Oyaizu, K. & Nishide, H. Aqueous electrochemistry of poly(vinylanthraquinone) for anode-active materials in high-density and rechargeable polymer/air batteries. *J. Am. Chem. Soc.* **133**, 19839–19843 (2011).
- Qin, H., Song, Z. P., Zhan, H. & Zhou, Y. H. Aqueous rechargeable alkali-ion batteries with polyimide anode. *J. Power Sources* **249**, 367–372 (2014).
- Huskinson, B. *et al.* A metal-free organic–inorganic aqueous flow battery. *Nature* **505**, 195–198 (2014).
- Janoschka, T. *et al.* An aqueous, polymer-based redox-flow battery using non-corrosive, safe, and low-cost materials. *Nature* **527**, 78–81 (2015).

21. Lin, K. *et al.* Alkaline quinone flow battery. *Science* **349**, 1529–1532 (2015).
22. Wei, X. *et al.* TEMPO-based catholyte for high-energy density nonaqueous redox flow batteries. *Adv. Mater.* **26**, 7649–7653 (2014).
23. Milczarek, G. & Inganäs, O. Renewable cathode materials from biopolymer/conjugated polymer interpenetrating networks. *Science* **335**, 1468–1471 (2012).
24. Novák, P., Müller, K., Santhanam, K. S. V. & Haas, O. Electrochemically active polymers for rechargeable batteries. *Chem. Rev.* **97**, 207–282 (1997).
25. Oyama, N., Tatsuma, T., Sato, T. & Sotomura, T. Dimercaptan–polyaniline composite electrodes for lithium batteries with high energy density. *Nature* **373**, 598–600 (1995).
26. Chung, W. *et al.* The use of elemental sulfur as an alternative feedstock for polymeric materials. *Nat. Chem.* **5**, 518–524 (2013).
27. Wang, J., Yang, J., Xie, J. & Xu, N. A novel conductive polymer–sulfur composite cathode material for rechargeable lithium batteries. *Adv. Mater.* **14**, 963–965 (2002).
28. Guo, W., Yin, Y.-X., Xin, S., Guo, Y.-G. & Wan, L.-J. Superior radical polymer cathode material with a two-electron process redox reaction promoted by graphene. *Energy Environ. Sci.* **5**, 5221–5225 (2012).
29. Janoschka, T. *et al.* Reactive inkjet printing of cathodes for organic radical batteries. *Adv. Energy Mater.* **3**, 1025–1028 (2013).
30. Walker, W. *et al.* Ethoxycarbonyl-based organic electrode for Li-batteries. *J. Am. Chem. Soc.* **132**, 6517–6523 (2010).
31. Han, X., Chang, C., Yuan, L., Sun, T. & Sun, J. Aromatic carbonyl derivative polymers as high-performance Li-ion storage materials. *Adv. Mater.* **19**, 1616–1621 (2007).
32. Chen, D. *et al.* A rigid naphthalenediimide triangle for organic rechargeable lithium-ion batteries. *Adv. Mater.* **27**, 2907–2912 (2015).
33. Chen, H. *et al.* Lithium salt of tetrahydroxybenzoquinone: toward the development of a sustainable Li-ion battery. *J. Am. Chem. Soc.* **131**, 8984–8988 (2009).
34. Jaffe, A., Valdes, A. S. & Karunadasa, H. I. Quinone-functionalized carbon black cathodes for lithium batteries with high power densities. *Chem. Mater.* **27**, 3568–3571 (2015).
35. Liang, Y., Zhang, P., Yang, S., Tao, Z. & Chen, J. Fused heteroaromatic organic compounds for high-power electrodes of rechargeable lithium batteries. *Adv. Energy Mater.* **3**, 600–605 (2013).
36. Castillo-Martínez, E., Carretero-González, J. & Armand, M. Polymeric Schiff bases as low-voltage redox centers for sodium-ion batteries. *Angew. Chem. Int. Ed.* **53**, 5341–5345 (2014).
37. Yao, M. *et al.* Indigo carmine: an organic crystal as a positive-electrode material for rechargeable sodium batteries. *Sci. Rep.* **4**, 3650 (2013).
38. Chen, R., Luo, R., Huang, Y., Wu, F. & Li, L. Advanced high energy density secondary batteries with multi-electron reaction materials. *Adv. Sci.* **3**, 1600051 (2016).
39. Wu, X. *et al.* Unraveling the storage mechanism in organic carbonyl electrodes for sodium-ion batteries. *Sci. Adv.* **1**, e1500330 (2015).
40. Skujins, S., Delderfield, J. & Webb, G. A. Spectroscopic and structural studies of some oxocarbon condensation products—II: a mass spectrometric study of some substituted phenazines and quinoxalines. *Tetrahedron* **25**, 3947–3954 (1969).
41. Burgstahler, A. W. & Barkhurst, R. C. Preparation of leuconic acid from inositol. *Trans. Kansas Acad. Sci.* **71**, 150–153 (1968).
42. Stephens, P. J., Devlin, F. J., Chabalowski, C. F. & Frisch, M. J. *Ab initio* calculation of vibrational absorption and circular dichroism spectra using density functional force fields. *J. Phys. Chem.* **98**, 11623–11627 (1994).
43. Becke, A. D. Density-functional thermochemistry. III. The role of exact exchange. *J. Chem. Phys.* **98**, 5648–5652 (1993).
44. Frisch, M. J. *et al.* *Gaussian 09, Revision A* (Gaussian, 2009).
45. Hehre, W. J., Ditchfie, R. & Pople, J. A. Self-consistent molecular-orbital methods. XII. Further extensions of gaussian-type basis sets for use in molecular-orbital studies of organic-molecules. *J. Chem. Phys.* **56**, 2257–2261 (1972).
46. Dill, J. D. & Pople, J. A. Self-consistent molecular-orbital methods. XV. Extended gaussian-type basis sets for lithium, beryllium, and boron. *J. Chem. Phys.* **62**, 2921–2923 (1975).
47. Francl, M. M. *et al.* Self-consistent molecular-orbital methods. XXIII. A polarization-type basis set for second-row elements. *J. Chem. Phys.* **77**, 3654–3665 (1982).
48. Miertuš, S., Scrocco, E. & Tomasi, J. Electrostatic interaction of a solute with a continuum. A direct utilization of *ab initio* molecular potentials for the prevision of solvent effects. *Chem. Phys.* **55**, 117–129 (1981).
49. Zhou, M. *et al.* High-performance silicon battery anodes enabled by engineering graphene assemblies. *Nano Lett.* **15**, 6222–6228 (2015).
50. Chung, K. Y., Yoon, W., Kim, K., Cho, B.-W. & Yang, X.-Q. Formation of an SEI on a LiMn₂O₄ cathode during room temperature charge–discharge cycling studied by soft X-ray absorption spectroscopy at the fluorine K-edge. *J. Appl. Electrochem.* **41**, 1295–1299 (2011).
51. Tasaki, K., Goldberg, A., Lian, J.-J., Walker, M., Timmons, A. & Harris, S. J. Solubility of lithium salts formed on the lithium-ion battery negative electrode surface in organic solvents. *J. Electrochem. Soc.* **156**, A1019–A1027 (2009).
52. Aurbach, D., Weissman, I. & Schechter, A. X-ray photoelectron spectroscopy studies of lithium surface prepared in several important electrolyte solution. A comparison with previous studies by Fourier transform infrared spectroscopy. *Langmuir* **12**, 3991–4007 (1996).
53. Li, W., Yao, H., Yan, K., Zheng, G., Chiang, Y.-M. & Cui, Y. The synergetic effect of lithium polysulfide and lithium nitrate to prevent lithium dendrite growth. *Nat. Commun.* **6**, 7436 (2015).
54. Schechter, A. & Aurbach, D. X-ray photoelectron spectroscopy study of surface films formed on Li electrodes freshly prepared in alkyl carbonate solutions. *Langmuir* **15**, 3334–3342 (1999).
55. Aurbach, D. *et al.* On the surface chemical aspects of very high energy density, rechargeable Li–sulfur batteries. *J. Electrochem. Soc.* **156**, A694 (2009).
56. Suo, L., Hu, Y.-S., Li, H., Armand, M. & Chen, L. A new class of solvent-in-salt electrolyte for high-energy rechargeable metallic lithium batteries. *Nat. Commun.* **4**, 1481 (2013).
57. Cheng, X.-B. *et al.* A review of solid electrolyte interphases on lithium metal anode. *Adv. Sci.* **3**, 1500213 (2016).

Acknowledgements

This work was supported by the National Research Foundation Investigator Award (NRF-NRF12015-01) ‘Graphene oxide – A new class of catalytic, ionic and molecular sieving materials’ funded by National Research Foundation, Prime Minister’s Office, Singapore. Y.Y. would like to acknowledge the financial support for their research at Xiamen University from National Natural Science Foundation of China (Grant Nos 21233004 and 21621091) and National Key Research and Development Program (Grant No. 2016YFB0901502).

Author contributions

C.P., J.S., C.S., Y.-S.H., Y.Y. and K.P.L. conceived and designed this work. J.S., C.P., G.-H.N. and D.Y. performed the syntheses and characterization of 2Q and 3Q materials, including ¹⁵N-labelled 3Q samples. G.-H.N. and B.T. prepared and characterized single-crystalline 3Q. C.P. and G.-H.N. conducted the EPR characterization. J.S. and C.P. assembled the cells for 2Q and 3Q and conducted the measurements. C.P. and G.Z. assembled the pouch cells for ¹⁵N-labelled 3Q and characterized the resource for ¹⁵N- and ¹³C-labelled 3Q during the charging/discharging processes. C.P., G.Z., Y.-S.H., M.-F.N., J.Y., M.A., Y.Y. and K.L. analysed the solid-state NMR results and proposed the mechanism. M.-F.N. conducted the DFT simulation. W.T. and J.S. performed TEM for 3Q samples after cycling. C.P. acquired high-resolution SRPES data. C.P., G.-H.N., L.Z., M.-F.N., J.Y., Y.-S.H., Y.Y., M.A. and K.P.L. co-wrote the manuscript. All the authors discussed the results and commented on the manuscript at all stages.

Additional information

Supplementary information is available for this paper.

Reprints and permissions information is available at www.nature.com/reprints.

Correspondence and requests for materials should be addressed to Y.Y. or K.P.L.

How to cite this article: Peng, C. *et al.* Reversible multi-electron redox chemistry of π -conjugated N-containing heteroaromatic molecule-based organic cathodes. *Nat. Energy* **2**, 17074 (2017).

Publisher’s note: Springer Nature remains neutral with regard to jurisdictional claims in published maps and institutional affiliations.

Competing interests

The authors declare no competing financial interests.